Exciton-impurity interactions in high-purity InP

R. Benzaquen
Institute for Microstructural Sciences, National Research Council of Canada, Ottawa, Ontario, Canada K1A OR6 and Département de Physique et Groupe de Recherche en Physique et Technologie des Couches Minces, Université de Montréal, Case Postale 6128, Succursale Centre-Ville, Montréal, Québec, Canada H3C 3J7

R. Leonelli
Département de Physique et Groupe de Recherche en Physique et Technologie des Couches Minces, Université de Montréal, Case Postale 6128, Succursale Centre-Ville, Montréal, Québec, Canada H3C 3J7

S. Charbonneau
Institute for Microstructural Sciences, National Research Council of Canada, Ottawa, Ontario, Canada K1A 0R6
(Received 11 May 1998; revised manuscript received 10 August 1998)

Temperature-dependent photoluminescence measurements have been performed to study the linewidth of the lower and upper polariton branches of the free-exciton transition in four high-purity *n*-type InP epilayers with a concentration of neutral shallow (deep) donors in the range of 7.9×10^{13}–2×10^{15} cm^{-3} [$(0-1.45)\times10^{14}$ cm^{-3}]. A line-shape analysis of the photoluminescence spectra revealed that the emission from upper-branch polaritons broadens rapidly when the temperature increases, while that of lower-branch polaritons displays a much smaller broadening in the corresponding temperature range. Moreover, when the concentration of neutral deep-donor centers is higher than that of neutral shallow donors, the emission linewidth from lower-branch polaritons exhibits a striking narrowing in the temperature range of 10–30 K. In addition, we have observed that the onset of emission linewidth narrowing from lower-branch polaritons shifts to lower temperatures as the neutral shallow-donor concentration is increased but kept below that of the neutral deep donors. In contrast, when the shallow-donor concentration is higher than that of the deep-donor centers, the emission linewidth narrowing from lower-branch polaritons vanishes. That behavior is similar to that obtained in a sample free of deep-donor centers, which at low temperatures does not display an emission linewidth narrowing of the lower polariton branch. Taken all together, our results cannot be explained within the framework of the standard polariton transport model, but are nevertheless well reproduced by a phenomenological model which takes into account polariton scattering by bound excitons, ionized impurities, and phonons. [S0163-1829(99)03703-0]

I. INTRODUCTION

In direct-gap III-V semiconductors such as InP or GaAs, exciton-photon interactions result in the formation of coupled modes called polaritons. The polariton dispersion curve in InP or GaAs can be described by a two-branch model:[1,2]

$$\epsilon(k,E)=\epsilon_b+\frac{4\pi\beta E_n^2(k)}{E_n^2(k)-E^2}, \tag{1}$$

$$E_n(k)=E_{n,T}+\frac{\hbar^2k^2}{2M}, \tag{2}$$

$$E_{n,\mathrm{LT}}=E_{n,L}-E_{n,T}=\left[\left(\frac{\epsilon_b+4\pi\beta}{\epsilon_b}\right)^{1/2}-1\right]E_{n,T}, \tag{3}$$

where k, E, and $\epsilon(k,E)$ are, respectively, the wave vector, energy, and dielectric function of the polariton. ϵ_b is the background dielectric constant without the polariton contribution, and M and β are, respectively, the total mass and polarizability of the exciton. $E_{n,T}$ and $E_{n,L}$ are, respectively, the nth transverse and nth longitudinal exciton energies. $E_{n,\mathrm{LT}}$ represents the nth longitudinal-transverse splitting energy which gives a measure of the coupling strength between the uncoupled longitudinal and transverse excitons at $k=0$. The values of those parameters for InP are given in Table I. Only the transverse exciton can interact with the electromagnetic field. The dispersion relation of the transverse polaritons is described by $\epsilon(k,E)=(\hbar ck/E)^2$, and that of the longitudinal polaritons by $\epsilon(k,E)=0$. Figure 1 shows the energy dispersion curves of InP for $n=1$. The upper polariton branch (UPB) begins at $E_{1,L}$ and quickly becomes photonlike at higher energies, while the lower polariton branch (LPB) becomes photonlike below $E_{1,T}$. For example, the lower-branch polaritons may be scattered by phonons into the energy region below or near $E_{1,T}$, where radiative decay of polaritons can take place through their photon components. In the course of that process, bottlenecking may occur whereby a quasithermal equilibrium of polaritons may be established, as first noted by Toyozawa.[3] As shown in the inset of Fig. 1, the group velocity of such lower-branch polaritons, $\nu_{\mathrm{LPB}}=\hbar^{-1}(dE_{\mathrm{LPB}}/dk)$, varies very rapidly with energy, and has a minimum at the bottleneck. Consequently, velocity-dependent scattering processes are expected to be greatly enhanced in that energy region. The existence of a propagating mode such as the polariton in the crystal has a profound effect upon the photoluminescence (PL) process,

TABLE I. Physical parameters of *n*-type InP. m^* and m^*_{hh} respectively, are the electron and heavy-hole masses, β is the polarizability of the exciton, and ϵ_s and ϵ_∞ are, respectively, the low and high dielectric constants. $E_{1,T}$ is the $n=1$ transverse exciton energy, T_o the temperature of the polar-optical phonons, ρ_m the mass density, E_1 the acoustical deformation potential, C_L the longitudinal speed of sound, p the piezoelectric coefficient, and E_{LO} the longitudinal-optical-phonon energy. $E_g(0)$ is the 0-K band gap, l and R are, respectively, the coefficients of the thermal expansion and compressibility, and $(\partial E_g/\partial P)_T$ is the variation of band gap with pressure.

m^* (a.u.)	0.082
m^*_{hh} (a.u.)	0.85
E_{LO} (meV)	42.8
$E_{1,T}$ (eV)	1.4185
E_1 (eV)	6.8
β	1.94×10^{-4}
$\epsilon_b=\epsilon_s$	12.38
ϵ_∞	9.55
T_o (K)	497
ρ_m (g/cm^3)	4.487
C_L (cm/s)	5.028×10^5
p	0.013
$E_g(0)$ (eV)	1.42
$3l/R(\partial E_g/\partial P)_T$ (eV/K)	5×10^{-5}

which must be viewed within the framework of a transport problem. Instead of a population of free excitons, which can recombine anywhere in the crystal producing photons that are free to exit the crystal unhindered, there is a population of polaritons that can produce external PL if the excitation first travels to the surface. In the polariton picture, a polariton impinging on the crystal interface has a certain probability of being transmitted as a photon and a certain probability of being reflected back. In particular, the low-temperature free-exciton PL of *n*-type GaAs with moderate donor concentration exhibits a dip at the energy corresponding to the exciton bottleneck, where the polariton group velocity is lowest (see the inset of Fig. 1). That dip, whose magnitude mostly depends on impurity concentration[4,5] and surface quality,[6,7] has been explained on the basis of polariton scattering by impurities or surface defects that prevent polaritons from reaching and escaping from the surface.[4,5] In samples with very low donor concentration ($N_D \leqslant 10^{15}$ cm^{-3}), the dip disappears and the free-exciton emission line shape becomes slightly asymmetrical, with a full width at half maximum (FWHM) of about 0.5 meV both in GaAs (Refs. 4 and 7) and InP.[8] Recently, however, free-exciton lifetime measurements[7] have cast some doubts on the use of the standard polariton transport model[3,4] to explain the kinetics of free-exciton recombination in direct-gap III-V semiconductors.

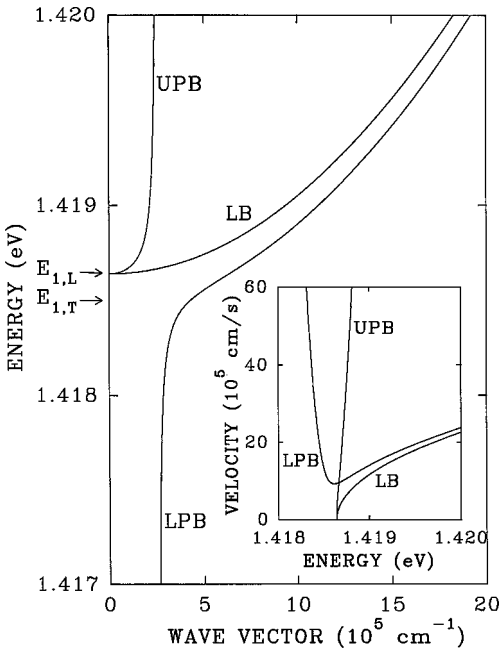

FIG. 1. Energy and group-velocity dispersion curves for the lower polariton branch (LPB), upper polariton branch (UPB), and longitudinal branch (LB), of *n*-type InP obtained using Eq. (1).

In order to understand better the optical mechanisms responsible for the emission linewidth of both the LPB and UPB components of the free-exciton transition, we have studied the free-exciton emission linewidth as a function of temperature in four high-purity, low-compensation, *n*-type InP epilayers. The present paper provides a detailed account of polariton phenomena that complements the preliminary results published recently on a high-purity *n*-type InP epilayer.[9] The paper is organized as follows. In Sec. II, we briefly describe the sample growth, the various experimental setups, and the low-field electronic transport analysis. Section III presents the PL and time-resolved photoluminescence (TRPL) data for our samples. Finally, Sec. IV presents the conclusions which can be drawn from this work.

II. EXPERIMENTS

The InP epilayers, samples 1–3, were grown by chemical beam epitaxy using phosphine (PH_3) and trimethylindium. Sample 4 was grown by low-pressure metal-organic chemical vapor deposition using PH_3 and triethylindium. The epilayers were deposited on (100) semi-insulating Fe-doped InP substrates oriented 2° off (100) toward ⟨110⟩. Details about the growth conditions are given elsewhere.[11,12] All the layers had a thickness of 5 μm as measured using a scanning electron microscope or an electrochemical profiler.

The optical measurements were carried out in a liquid-helium flow cryostat with the samples mounted strain free on a Cu block. The temperature of the sample holder could be varied between 4.2 and 300 K with an accuracy of ±0.1 K. The PL was excited using a HeNe laser, dispersed by a 0.64-m spectrometer, and detected by a liquid-nitrogen-cooled charge-coupled device. The pulse excitation for the TRPL experiments was provided by a mode-locked Nd^{3+}:YAG (yttrium aluminum garnet) laser pumping a Rhodamine 640 dye laser. The resulting 5-ps pulses were at a wavelength of 620 nm; and the repetition rate was set to 4 MHz in order to extend the time range. The transient PL measurements were carried out using a delayed coincidence photon-counting system. The instrumental response of that system had an exponential decay of 100 ps. The spectral resolution and excitation power density were set, respec-

TABLE II. Results obtained from the analysis of four *n*-type InP samples. N_{D_1}, N_{D_2}, and N_A are, respectively, the shallow-donor, deep-donor, and acceptor concentrations. σ_{D_2} is the standard deviation of the band of deep donors, centered at the binding energy $E_{D_2}^c$. E_{D_1} is the shallow-donor binding energy. n_{D_1} and μ_{D_1}, are, respectively, the electronic concentration and mobility in the shallow-donor band.

No.	N_{D_1} (cm^{-3})	N_{D_2} (cm^{-3})	N_A (cm^{-3})	σ_{D_2} (meV)	E_{D_1} (meV)	$E_{D_2}^c$ (meV)	μ_{D_1} (cm^2 V^{-1} s^{-1})	n_{D_1} (cm^{-3})
1	7.9×10^{13}	1.39×10^{14}	3.7×10^{13}	70	7	160	903	2.9×10^{13}
2	1.38×10^{14}	2.0×10^{14}	7.3×10^{13}	65	7	160	2251	1.21×10^{13}
3	1.82×10^{14}	1.45×10^{14}	6.8×10^{13}	75	7	160	580	1.35×10^{14}
4	2.0×10^{15}		2.48×10^{14}		6		652	2.51×10^{13}

tively, at 0.04 meV and 1 W/cm^2 for all the optical measurements.

A detailed account of the low-field electronic transport measurements performed on samples 1–3 was recently published.[8,10] Sample 4 (the deep-donor free sample) was shaped in a standard multiarm bridge configuration, and Au-Ge contacts were deposited and annealed at 450 SDC. All contacts were checked for linearity of the current-voltage (*I-V*) characteristics and the sample had excellent uniformity, as verified with voltage readings across the various contacts. To avoid temperature gradients between the sample and the alumina holder, the temperature was varied without heat supply, rising slowly from the lowest temperature. The data were collected with a precision high-impedance data acquisition system[13] under low-electric-field (20 mV/cm) and low-magnetic-field (1 kG) conditions. The analysis of the low-field electronic transport data was performed using the iterative solution to the Boltzmann equation due to Rode,[14] and the material parameters reported in Table I. A detailed account of the low-field electronic transport analysis carried out on samples 1–3 is reported elsewhere.[8,10] The low-field electronic transport analysis of sample 4 has been carried out using a procedure identical to that of samples 1–3 (not shown). Table II presents the results obtained from the analysis of the low-field electronic transport data. We point out that the uncertainties of the parameters quoted in Table II fell significantly below 5% for all samples. As shown in Table II, our samples are characterized by a shallow-donor band centered at $E_{D_1}=6$ or 7 meV, whose width can be estimated to 1% of E_{D_1}.[15] In addition to an extremely narrow shallow-donor band where both disorder and strong Coulomb interactions play crucial roles in the electrical conduction, samples 1–3 are characterized by a broadband of localized deep-donor centers centered at $E_{D_2}^c=160$ meV below the conduction-band edge, with a FWHM of about 165 meV.[8,10,16]

III. PHOTOLUMINESCENCE AND TIME-RESOLVED PHOTOLUMINESCENCE

The near-band edge PL of direct-gap III-V semiconductor compounds such as InP or GaAs is usually dominated at liquid-helium temperatures by bound and free excitonic transitions. Due to the exciton localization around the binding centers, bound-excitonic (BE) complexes give usually narrow PL line shapes, in sharp contrast with the much broader free-exciton emission. It is widely believed that the emission linewidth of free excitons is well understood. However, so far, little effort has been devoted to the accurate description as a function of temperature of the emission linewidth of both the LPB and UPB components of the free-exciton transition.

The free-exciton emission linewidth γ_i ($i=$LPB or UPB) in a bulk III-V semiconductor such as InP or GaAs can be expressed as[9,17,18]

$$\gamma_i(T)=\gamma(0)+\gamma_I+\gamma_{\rm BE}+\gamma_A+\gamma_O\,. \tag{4}$$

The first term in Eq. (4), $\gamma(0)$, represents the intrinsic linewidth, and is determined at the lowest temperatures by several scattering processes such as exciton-exciton scattering, exciton-carrier scattering or carrier-carrier scattering. The second term in Eq. (4), γ_I, arises from scattering due to ionized impurities and is given by[8,10]

$$\gamma_I(T)=\sum_{i=1}^{2}\gamma_{D_i^+}=\sum_{i=1}^{2}\Gamma_{D_i^+}N_{D_i}^+, \tag{5}$$

$$N_{D_1}^+=\frac{N_{D_1}}{1+2\exp\left(\dfrac{E_F-E_{D_1}}{k_BT}\right)}, \tag{6}$$

$$N_{D_2}^+=N_{D_2}-\int_{-\infty}^{+\infty}G_{D_2}(E)f_0(E)dE, \tag{7}$$

$$G_{D_2}(E)=\frac{N_{D_2}}{\sqrt{2\pi}\sigma_{D_2}}\exp\left[-\frac{1}{2}\left(\frac{E-E_{D_2}^c}{\sigma_{D_2}}\right)^2\right], \tag{8}$$

$$f_0(E)=\frac{1}{1+\dfrac{1}{2}\exp\left(\dfrac{E-E_F}{k_BT}\right)}, \tag{9}$$

where $N_{D_i}^+$ is the concentration of ionized shallow ($i=1$) or deep ($i=2$) donors, and $\Gamma_{D_i}^+$ is their associated broadening cross section, to be determined from our data analysis. N_{D_i} is the concentration of neutral shallow ($i=1$) or deep ($i=2$) donors, $G_{D_2}(E)$ is the density of states of the band of localized deep donors, taken in a first approximation as a Gaussian distribution normalized to N_{D_2} and centered at $E_{D_2}^c$, with

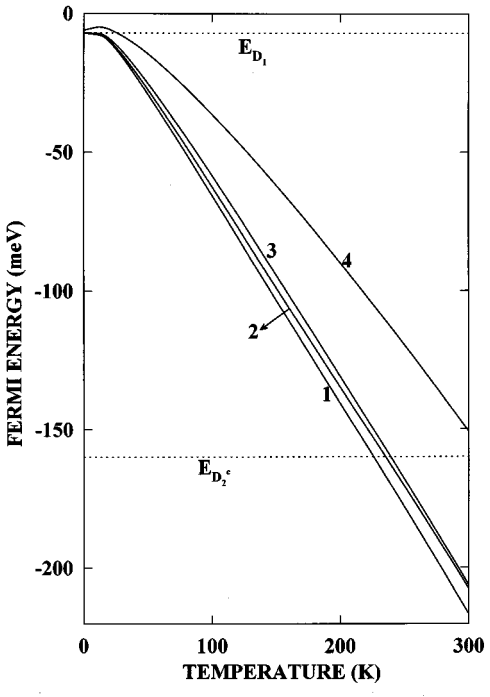

FIG. 2. Fermi energy as a function of temperature for samples 1–4. E_{D_1} is the shallow-donor binding energy. $E_{D_2^c}$ is the binding energy of the center of the deep-donor band.

a standard deviation σ_{D_2}. $f_0(E)$ represents the Fermi-Dirac distribution function. The computation of γ_I requires the evaluation of the Fermi energy E_F through the numerical solution of the neutrality equation

$$n_c - \sum_{i=1}^{2} N_{D_i}^{+} + N_A = 0, \tag{10}$$

$$n_c = \int_{E_c}^{+\infty} G_c(E) f_0(E) dE, \tag{11}$$

$$G_c(E) = \frac{4md}{h^2} k, \tag{12}$$

$$k = \left(\frac{mE_g}{\hbar^2} \left\{ \frac{m}{m^*} + \frac{2E}{E_g} - \left[\left(\frac{m}{m^*} \right)^2 + \frac{4E}{E_g} \left(\frac{m}{m^*} - 1 \right) \right]^{1/2} \right\} \right)^{1/2}, \tag{13}$$

$$d = \frac{1}{1 + \left(\frac{m}{m^*} - 1 \right) \alpha^{-1}}, \tag{14}$$

$$\alpha = \left[1 + \frac{2\hbar^2 k^2}{E_g} \left(\frac{1}{m^*} - \frac{1}{m} \right) \right]^{1/2}, \tag{15}$$

where n_c is the concentration of free electrons, $G_c(E)$ the density of states of the conduction band, E_c the energy of the bottom of the conduction band, and E_g the temperature-dependent band gap. m and m^* are, respectively, the free-electron mass and the electron effective masses. Figure 2 presents E_F as a function of temperature for our samples. The calculations have been referenced with respect to the bottom of the conduction band. As the temperature increases, E_F falls deeper into the energy gap and eventually reaches within a few $k_B T$ of the shallow- and deep-donor centers. At that point, the donor centers begin to ionize. When the deep-donor centers are taken into account in our model (samples 1–3), we observe a faster rate of fall of E_F into the band gap. We point out that the band of deep-donor centers is not completely ionized at room temperature, as evidenced by the 300-K E_F value of about 225 meV.

The third term in Eq. (4), γ_{BE}, is due to the scattering of polaritons by localized excitons. Such an interaction has been shown recently to control the low-temperature emission linewidth of high-purity n-type InP (Ref. 9) and of GaAs/Ga_xAl_{1-x}As multiple quantum wells.[18] The temperature dependence of γ_{BE} should be proportional to the concentration of bound excitons:[19]

$$\gamma_{\mathrm{BE}}(T) = \sum_{i=1}^{2} \gamma_{\mathrm{BE}_i} = \sum_{i=1}^{2} \gamma_{(B,X)_i} N_{\mathrm{BE}_i}, \tag{16}$$

$$N_{\mathrm{BE}_i} = \frac{N_{D_i}}{1 + C_{(B,X)_i} T^{3/2} \exp\left[-\frac{E_{B,X}}{k_B T} \right]}, \tag{17}$$

$$C_{(B,X)_i} = \left(\frac{2\pi M k_B}{h^2 N_{D_i}^{2/3}} \right)^{3/2}, \tag{18}$$

where N_{BE_i} is the concentration of shallow ($i=1$) or deep ($i=2$) donor bound excitons, and $\gamma_{(B,X)_i}$ is their associated bound-exciton broadening cross section. $E_{B,X}$ is the exciton localization energy, and $C_{(B,X)_i}$ a constant linked to the concentration of binding centers N_{D_i}. The parameters $\gamma_{(B,X)_i}$ and $E_{B,X}$ will be determined from our data analysis.

The remaining terms in Eq. (4), γ_A and γ_O, are due, respectively, to the interaction of excitons with the LA- and LO-phonon modes of the lattice, and are given by[17]

$$\gamma_A(T) = \gamma_{\mathrm{LA}} T, \tag{19}$$

$$\gamma_O(T) = \frac{\gamma_{\mathrm{LO}}}{\exp\left(\frac{E_{\mathrm{LO}}}{k_B T} \right) - 1}, \tag{20}$$

where γ_{LA} and γ_{LO} are, respectively, the LA coefficient and the LO linewidth parameter, to be determined from our data analysis, and E_{LO} is the LO-phonon energy of InP (see Table I).

Figures 3–6 display, for samples 1–4, the temperature dependence of the PL spectra in the excitonic region. For clarity, the spectra corresponding to each sample have been normalized to the same maximum value. The PL spectra exhibit apparent similar optical features. At the lowest temperature, the PL spectra are characterized by sharp neutral shallow-donor–bound-excitonic transitions $(D_1^0,X)_n$ (e.g., structures $d-g$ of Fig. 3), and by the LPB of the $n=1$ free-exciton (FE_1) transition (e.g., structure c of Fig. 3). The shoulder observed at higher photon energy is attributed to the UPB of the FE_1 transition (e.g., structure b of Fig. 3). Although the origin of the excited states of the (D_1^0,X) com-

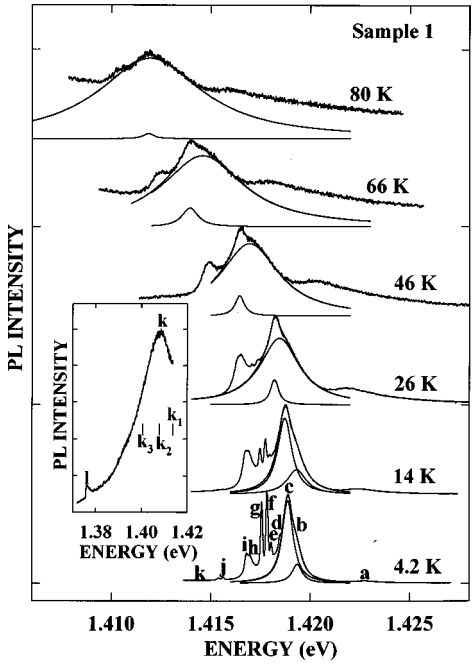

FIG. 3. Temperature-dependent PL spectra of *n*-type InP (sample 1). $a=\mathrm{FE}_2$ is the $n=2$ free-exciton transition. *b* and *c* are, respectively, the UPB and LPB components of the FE_1 transition; *d*–*g* are the neutral shallow-donor–bound-excitonic transitions $(D_1^0,X)_n$; $h=(D_1^0,h)$ is the neutral shallow-donor to free-hole recombination; $i=(D_1^+,X)$ is the ionized shallow-donor–bound-excitonic transition; $j=(A^0,X)$ is the neutral acceptor–bound-excitonic transition; $k=(D_2^0,X)$ is the neutral deep-donor–bound-excitonic transition; and $1=(D_1^0,A^0)$ is the neutral shallow-donor–acceptor pair recombination. The solid curves are Lorentzian fits to structures *b* and *c*.

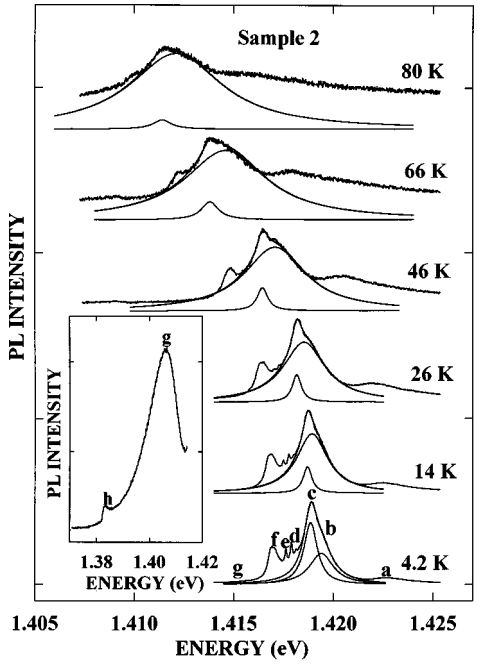

FIG. 4. Temperature-dependent PL spectra of *n*-type InP (sample 2). $a=\mathrm{FE}_2$ is the $n=2$ free-exciton transition. *b* and *c* are, respectively, the UPB and LPB components of the FE_1 transition; *d* and *e* are, respectively, the $n=1$ and 2 parts of the neutral shallow-donor–bound-excitonic transitions $(D_1^0,X)_n$; *f* is a combination of a neutral shallow donor to free-hole recombination (D_1^0,h) with an ionized shallow-donor–bound-excitonic transition (D_1^+,X); $g=(D_2^0,X)$ is the neutral deep-donor–bound-excitonic transition; and $h=(D_1^0,A^0)$ is the neutral shallow-donor–acceptor pair recombination. The solid curves are Lorentzian fits to structures *b* and *c*.

plex is still controversial, they are usually attributed to different angular momentum states of the $J=\frac{3}{2}$ hole characteristic of the valence-band maximum.[20] We point out that sample 4, which is characterized by a value of N_{D_1} much higher than that of samples 1–3 (see Table II), displays a 4.2-K PL spectrum where the $(D_1^0,X)_n$ transitions dominate over the FE_1 emission peak, as shown in Fig. 6. In contrast, the 4.2-K PL spectra of samples 1–3 are dominated at high photon energies by strong FE_1 emissions, as shown in Figs. 3–5. Those high-quality optical features are linked to the electrical characteristics of samples 1–3, which consist of depressed 300-K Hall mobility (μ_H) values (well below 6×10^3 cm^2 V^{-1} s^{-1}) and of exceptionally high low-temperature μ_H peak values (well above 2×10^5 cm^2 V^{-1} s^{-1}). As already mentioned, detailed electronic transport and optical studies[8,10,15] recently carried out on samples 1–3 revealed the presence of a broadband of localized deep-donor centers extending into the gap. Linked to the presence of that band, a bound-excitonic PL band (D_2^0,X) with a FWHM of about 22 meV was observed between the acceptor–bound-excitonic (A^0,X) doublet transition and the neutral shallow-donor–acceptor pair recombination (D_1^0,A^0) (e.g., structure *k* in the inset of Fig. 3). As expected, sample 4, which is free of deep donor centers (see Table II), does not exhibit any PL optical structure located between the (A^0,X) doublet transition and the (D_1^0,A^0) pair recombination, as shown in the inset of Fig. 6.

The slightly asymmetrical 4.2-K FE_1 emission line shapes shown in Figs. 3–6 indicate semiconductor crystals with a low concentration of donors (see Table II). As displayed in Figs. 3–6, with increasing temperature, the PL intensities of the $(D_1^0,X)_n$ complexes are drastically reduced with respect to those of the FE_1 transitions due to the thermal dissociation of the $(D_1^0,X)_n$ complexes. In particular, the $(D_1^0,X)_{n=1}$ and $(D_1^0,X)_{n=2}$ complexes are known to dissociate through two dissociation paths.[21] When the temperature is increased to about 8 K, the dominating dissociation process results in the liberation of free excitons from shallow donors. When the temperature is further increased to 20 K, the liberation of free electrons and free holes is responsible for the dissociation of the $(D_1^0,X)_{n=1}$ and $(D_1^0,X)_{n=2}$ complexes. In contrast, the temperature dependence of the FE_1 transition is quite intriguing. As shown in Figs. 3–6, with increasing temperature, the FE_1 emission line shapes can be seen as the sum of a narrow and a broad component. That is particularly evident in the spectrum taken at 46 K of, for example, sample 1. As in a previous work,[9] to quantify that effect, we have empirically chosen a sum of two Lorentzians to take into account both the LPB and UPB emissions

$$I(E)=\sum_{i=\mathrm{LPB,UPB}}\frac{I_i}{1+\left(\dfrac{E-E_{i,c}}{\gamma_i}\right)^2}, \tag{21}$$

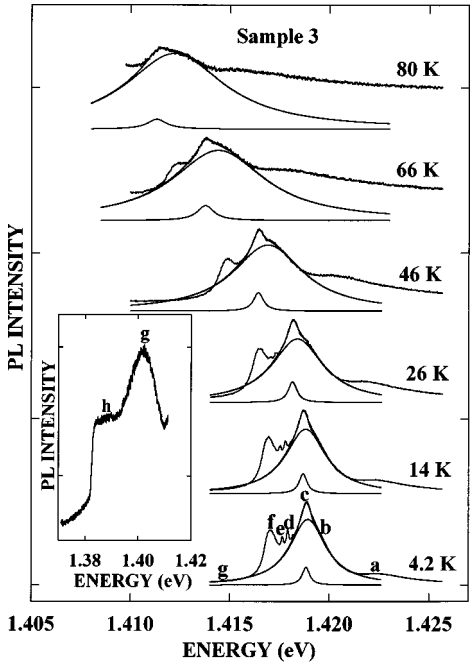

FIG. 5. Temperature-dependent PL spectra of *n*-type InP (sample 3). $a = \mathrm{FE}_2$ is the $n=2$ free-exciton transition. *b* and *c* are, respectively, the UPB and LPB components of the FE_1 transition; *d* and *e* are, respectively, the $n=1$ and 2 parts of the neutral shallow-donor–bound-excitonic transitions $(D_1^0,X)_n$; *f* is a combination of a neutral shallow-donor to free-hole recombination (D_1^0,h) with an ionized shallow-donor–bound-excitonic transition (D_1^+,X); $g=(D_2^0,X)$ is the neutral deep-donor–bound-excitonic transition; and $h=(D_1^0,A^0)$ is the neutral shallow-donor–acceptor pair recombination. The solid curves are Lorentzian fits to structures *b* and *c*.

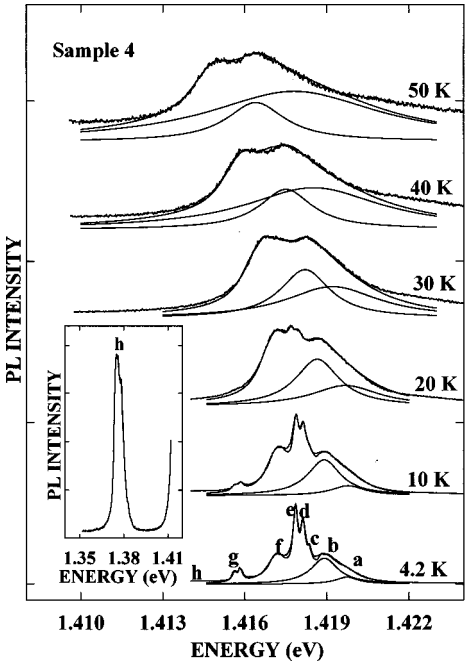

FIG. 6. Temperature-dependent PL spectra of *n*-type InP (sample 4). *a* and *b* are, respectively, the UPB and LPB components of the FE_1 transition; *c*–*e* are the neutral shallow-donor–bound-excitonic transitions $(D_1^0,X)_n$; *f* is a combination of a neutral shallow-donor to free-hole recombination (D_1^0,h) with an ionized shallow-donor–bound-excitonic transition (D_1^+,X); $g=(A^0,X)$ is the neutral acceptor–bound-excitonic transition; and $h=(D_1^0,A^0)$ is the neutral shallow-donor–acceptor pair recombination. The solid curves are Lorentzian fits to structures *a*–*g*.

where the *i*th Lorentzian line shape of intensity I_i is centered at the photon energy $E_{i,c}$, with a half-width at half maximum γ_i. The results of an iterative least-squares fit to the normalized PL data using Eq. (21) are also shown in Figs. 3–6. For samples 1–3, the least-squares calculation has been carried out in an energy interval carefully chosen around $E_{i,c}$ to minimize contributions from neighboring transitions to the overall line shape of the FE_1 transition. In contrast, the FE_1 emission peak of sample 4 is significantly affected by neighboring transitions such as the $(D_1^0,X)_n$ recombinations. The results of fits for sample 4 which take into account all relevant near-band-edge transitions contributing to the PL spectra are also shown in Fig. 6. The agreement between experimental and theoretical line shapes for samples 1–4 is excellent in the temperature range of 4.2–80 K. We point out that the PL measurements for sample 4 were performed in the temperature range of 4.2–50 K to avoid excessive broadening of the LPB and UPB components of the FE_1 transition which could lead to an inaccurate determination of γ_i at high temperatures.

Figure 7 presents for samples 1–4 the temperature dependencies of the photon energies $E_{\mathrm{LPB},c}$ (triangles) and $E_{\mathrm{UPB},c}$ (circles). As shown in Fig. 7, $E_{\mathrm{LPB},c}$ and $E_{\mathrm{UPB},c}$ follow the temperature dependence (with $E_{\mathrm{LPB},c} < E_{\mathrm{UPB},c}$ in the temperature range of 4.2–80 K) predicted by the well-known Varshni equation[22]

$$E_{i,c}(T) = E_{i,c}(0) - \frac{\alpha_i T^2}{(\beta_i + T)}, \tag{22}$$

where $E_i(0)$, α_i, and β_i are assumed to be adjustable parameters ($i=$ LPB or UPB). The solid lines of Fig. 7 have been generated using Eq. (22) with the parameters $E_i(0)$, α_i, and β_i quoted in Table III.

In Figs. 8–11, for samples 1–4 we display the temperature dependencies of the experimental linewidths γ_{LPB} and γ_{UPB} of the FE_1 transitions. As shown in Figs. 8–11, γ_{UPB} increases more rapidly as a function of temperature than γ_{LPE}. In addition, samples 1 and 2 exhibit an initial increase of γ_{LPB} followed by an abrupt decrease at $\approx$25 and 15 K, respectively. In contrast, samples 3 and 4 do not show such a reduction of γ_{LPB} at low temperatures, as displayed in Figs. 10 and 11. The standard polariton transport model from Ref. 4 is insufficient to explain the temperature dependencies of γ_{LPB} and γ_{UPB} shown in Figs. 8–11. That model is based on a single scattering mechanism (neutral impurities) which operates at the lowest temperatures. The effects that we observe span over a broad temperature range (4.2–80 K), where several scattering mechanisms affect the polariton emission line shape. In addition, the standard polariton transport model cannot explain the existence of two independent Lorentzian distributions describing, in a broad temperature range, the emission line shapes of both the LPB and UPB components of the FE_1 transition. Moreover, the behaviors of γ_{LPB} and γ_{UPB} at high temperatures (see Figs. 8–11) indicate that UPB emission can be observed in the same energy range as LPB emission. That observation is incompatible with the standard polariton transport model, which requires that the high-energy part of the FE_1 emission be composed of upper-

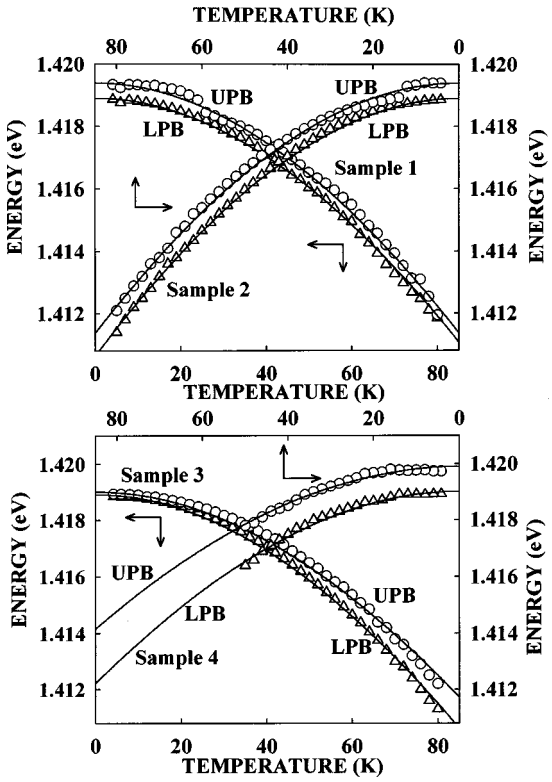

FIG. 7. Temperature dependencies of the photon energies $E_{\mathrm{LPB},c}$ (triangles) and $E_{\mathrm{UPB},c}$ (circles) of *n*-type InP (samples 1–4). The solid lines represent fits obtained using Eq. (22).

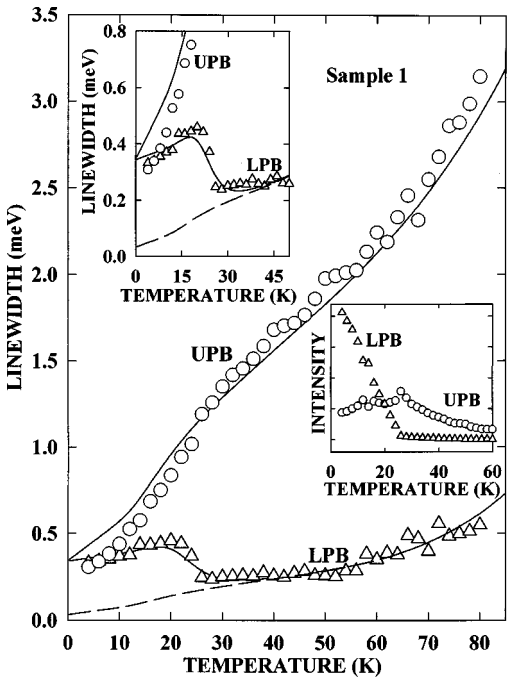

FIG. 8. Temperature dependencies of the linewidths γ_{LPB} (triangles) and γ_{UPB} (circles) of *n*-type InP (sample 1). The solid lines represent the full theoretical calculations obtained using Eq. (4) for the LPB and UPB, respectively. The dashed line is the theoretical calculation when bound-exciton scattering is not taken into account. The bottom right-hand inset displays the temperature dependencies of the integrated PL intensities of structures *b* (circles) and *c* (triangles) of Fig. 3.

branch polaritons and the low-energy part of lower-branch polaritons, with some admixture of both types of polaritons in a narrow energy range near $E_{1,L}$.[5]

In the insets of Figs. 8–11, we display the temperature dependencies of the integrated intensities I^*_{LPB} and I^*_{UPB}. Regarding samples 1 and 4, at the lowest temperatures, most of the polariton population resides in the bottleneck region of the LPB. As the temperature is raised to ≈25 K, I^*_{LPB} decreases very rapidly while I^*_{UPB} increases. That indicates that there exists an energy-transfer path whereby, for a given energy, the lower-branch polariton population is converted into upper-branch polaritons as the temperature is increased to ≈25 K. We point out that the polariton population transfer observed from the LPB to the UPB with increasing temperature cannot be explained by thermal excitation, since at the lowest temperatures the densities of states of both polariton populations span the same energy range. Regarding sample 2, $I^*_{\mathrm{LPB}} \approx I^*_{\mathrm{UPB}}$ for temperatures below ≈12 K, which indicates that at low temperatures both lower- and upper-branch polariton populations do not fluctuate significantly with temperature, and are approximately equal to each other. However, when the temperature is raised above ≈12 K, I^*_{LPB} abruptly decreases while I^*_{UPB} sharply increases and then decreases. Finally, as shown in the inset of Fig. 10, sample 3 exhibits a decrease of both I^*_{LPB} and I^*_{UPB} for temperatures above 4.2 K. However, the rate of decrease of I^*_{UPB} with temperature is much faster than that of I^*_{LPB}, as displayed in the inset of Fig. 10.

TABLE III. Parameters $E_{i,c}(0)$, α_i, and β_i of Varshni's Eq. (22) obtained for four InP samples.

	$E_{i,c}(0)$ (eV)	α_i (10^{-4} eV K^{-1})	β_i (K)
No. 1			
LPB	1.4189	7.7	625
UPB	1.4194	7.4	580
No. 2			
LPB	1.4189	8	615
UPB	1.4194	7.5	635
No. 3			
LPB	1.4189	7.4	560
UPB	1.4190	6.7	580
No. 4			
LPB	1.4190	7.6	725
UPB	1.4199	9.8	1150

The solid lines of Figs. 8–11 have been generated using Eq. (4) with the physical material parameters of InP presented in Table I and the parameters reported in Table II which have been extracted from the low-field electronic transport analysis. The results of the fits are reported in Table IV. We point out that γ_{LPB} and γ_{UPB} of all our samples have been consistently fitted using Eq. (4) with the same values of $\gamma(0)$, γ_{LA}, and γ_{LO}. As shown in Figs. 8–11, the overall agreement between the experimental data and the theoretical calculation is excellent in the temperature range of 4.2–80 K. The discrepancies observed between experimental data and the theoretical calculation for samples 3 and 4 can be cor-

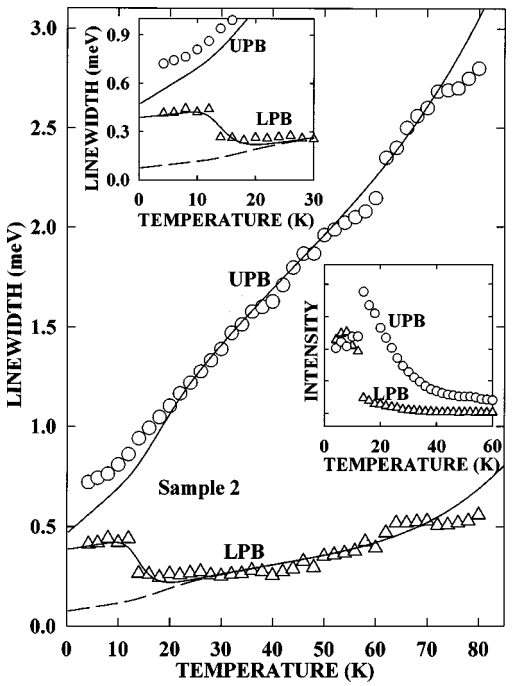

FIG. 9. Temperature dependencies of the linewidths γ_{LPB} (triangles) and γ_{UPB} (circles) of *n*-type InP (sample 2). The solid lines represent the full theoretical calculations obtained using Eq. (4) for the LPB and UPB, respectively. The dashed line is the theoretical calculation when bound exciton scattering is not taken into account. The bottom right-hand inset displays the temperature dependencies of the integrated PL intensities of structures *b* (circles) and *c* (triangles) of Fig. 4.

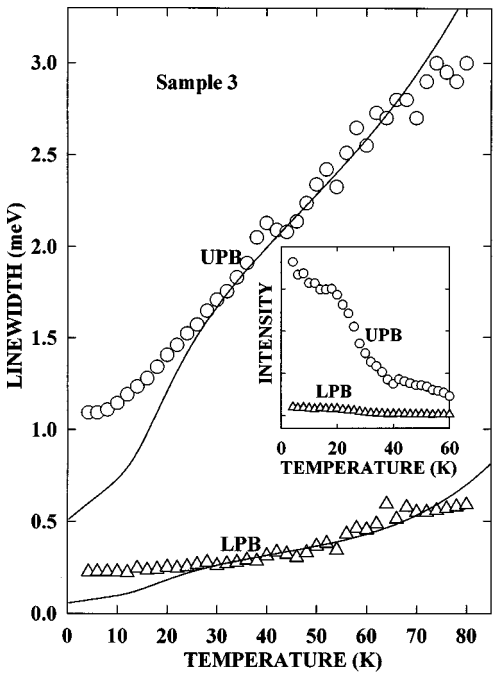

FIG. 10. Temperature dependencies of the linewidths γ_{LPB} (triangles) and γ_{UPB} (circles) of *n*-type InP (sample 3). The solid lines represent the full theoretical calculations obtained using Eq. (4) for the LPB and UPB, respectively. The inset displays the temperature dependencies of the integrated PL intensities of structures *b* (circles) and *c* (triangles) of Fig. 5.

rected by letting $\gamma(0)$, γ_{LA}, and γ_{LO} vary somewhat from sample to sample. It is to be noted that $\gamma_{(B,X)_2}$ and $C_{(B,X)_2}$ can be determined independently from the other parameters by using the variation of γ_{LPB} in the temperature range of $\approx$4.2–35 K. The dashed lines of Figs. 8 and 9, which have been generated using Eq. (4) with $\gamma_{\mathrm{BE}_2}=0$, fail to reproduce the low-temperature behavior of γ_{LPB}. However, when the polariton interaction with (D_2^0,X) complexes is taken into account, the model reproduces the observed net linewidth narrowing of the LPB for samples 1 and 2. That effect, which is not observed in samples 3 and 4, is due to the vanishing of polariton scattering from (D_2^0,X) complexes, as shown by the fitted values of $E_{B,X}$ quoted in Table IV. The value of $E_{B,X}=15.8$ meV for sample 1 corresponds to the spectral region near the low-energy side of the (D_2^0,X) emission band (see the inset of Fig. 3). In contrast, the value of $E_{B,X}=8.6$ meV for sample 2 corresponds to the spectral region near the high-energy side of the (D_2^0,X) emission band (see the inset of Fig. 4), and seems to be linked to a population of shallower (D_2^0,X) complexes.

The qualitative understanding of the temperature behaviors of γ_{LPB} for samples 1–4 requires some discussion about bound-exciton formation. It is well known that the binding energy of an exciton can be decreased by the presence of an impurity. Whether or not an exciton can be trapped on an impurity is determined by the interplay of several competing effects: energy, impurity concentration, and temperature. If the total energy of the system is reduced when the exciton is in the vicinity of an impurity and the temperature sufficiently

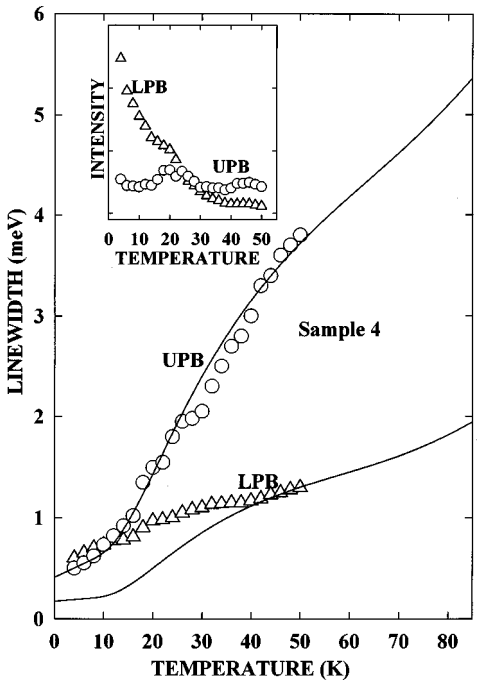

FIG. 11. Temperature dependencies of the linewidths γ_{LPB} (triangles) and γ_{UPB} (circles) of *n*-type InP (sample 4). The solid lines represent the full theoretical calculations obtained using Eq. (4) for the LPB and UPB, respectively. The inset displays the temperature dependencies of the integrated PL intensities of structures *a* (circles) and *b* (triangles) of Fig. 6.

TABLE IV. Parameters of Eq. (4) extracted from the temperature dependencies of the emission linewidths corresponding to the LPB and UPB of four *n*-type InP samples. $\Gamma_{D_i^+}$ is the broadening cross section of the ionized shallow ($i=1$) or deep ($i=2$) donor center. $\gamma(0)$, γ_{LA}, and γ_{LO}, respectively, are the intrinsic linewidth, the longitudinal acoustical coefficient, and the longitudinal-optical linewidth parameter. $\gamma_{(B,X)_2}$ is the deep-donor bound-exciton broadening cross section, and $E_{B,X}$ the exciton localization energy.

	$\Gamma_{D_1^+(D_2^+)}$ (10^{-15} meV cm^3)	$\gamma(0)$ (meV)	$\gamma_{(B,X)_2}$ (10^{-15} meV cm^3)	$E_{B,X}$ (meV)	γ_{LA} (10^{-2} meV K^{-1})	γ_{LO} (meV)
No. 1						
LPB	1 (−)		2.23	15.8	0.41	106
UPB	6 (40)				2.3	138
No. 2						
LPB	1.1 (−)		1.6	8.6	0.41	106
UPB	4.5 (35)				2.3	138
No. 3						
LPB	0.9 (−)				0.41	106
UPB	5 (40)				2.3	138
No. 4						
LPB	0.7 (−)				0.41	106
UPB	1.65 (−)				2.3	138

low, it will be energetically more favorable for the exciton to bind around the impurity and form a bound exciton. In our case, the situation is complicated by the presence of two competing binding populations, the shallow- and deep-donor populations, whose PL cover a broad $E_{B,X}$ spectral range (from the edge of the conduction band to ≈39 meV below the conduction band). For example, if the value of N_{D_1} is sufficiently high with respect to that of N_{D_2}, excitons will start to favor binding around the shallower donor centers rather than around the deeper ones. However, as pointed out in Ref. 23, the boundary between excitons bound to shallow and deep impurities is difficult to define. That is due to the fact that $E_{B,X}$ is not necessarily a reliable measure of the degree of localization of wave functions dominated by short-range forces. As shown in Figs. 8 and 9, when the value of N_{D_1} is increased sufficiently but kept below that of N_{D_2} (see Table II), it becomes more favorable for the excitons to start binding around an increasingly larger number of relatively shallower donor centers, as evidenced by the shift to lower temperatures of the onset of emission linewidth narrowing from lower-branch polaritons. In addition, as shown in Fig. 10 for sample 3, when N_{D_1} is increased significantly above the value of N_{D_2} (see Table II), the emission linewidth narrowing from lower-branch polaritons vanishes. It is then reasonable to speculate that for sample 3 most of the excitons are bound around the shallowest donor centers. That interpretation of the data is supported by the low-temperature behaviour of γ_{LPB} for sample 4 ($N_{D_2}=0$), which exhibits no reduction of γ_{LPB} at low temperatures, as shown in Fig. 11. Additional evidence of the favored exciton interaction with shallower deep-donor centers in our samples can also be provided by TRPL measurements performed across the (D_2^0,X) emission band.

The description of the dynamical relaxation process in a III-V bulk semiconductor such as InP is quite complex.[24] A photoexcited electron and hole can form an exciton by interaction with acoustical and optical phonons, and also by carrier-carrier interactions. The relaxation of photoexcited pairs within the bands proceeds simultaneously with the exciton formation process. In order to describe the transient PL behavior of our samples, let us consider the four-level system depicted in Fig. 12. The system is pumped from the ground level $|0\rangle$ to the level $|e\text{-}h\rangle$, where a population of electron-hole pairs is established. Moreover, we shall only consider the PL signal from the free-exciton $|\mathrm{FE}\rangle$ and bound-exciton $|\mathrm{BE}\rangle_s$ levels, where the subscript s stands for the sth bound-exciton level. On the one hand, the $|\mathrm{FE}\rangle$ level can be

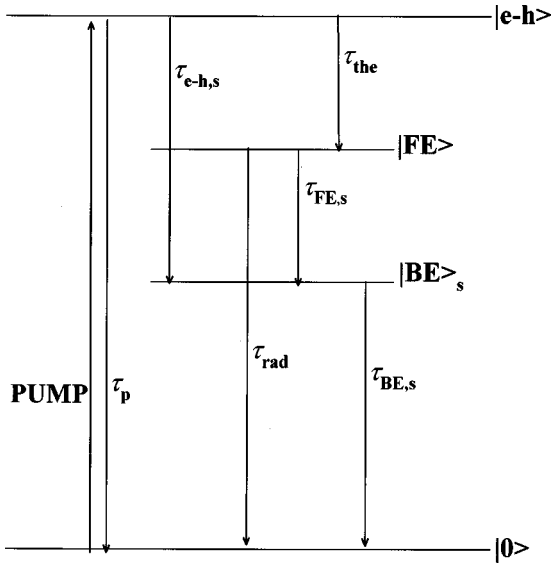

FIG. 12. Schematics of a four-level system. $|0\rangle$, $|e\text{-}h\rangle$, $|\mathrm{FE}\rangle$, and $|\mathrm{BE}\rangle_s$ represent, respectively, the ground, electron-hole-pair, free-exciton, and bound-exciton levels. The index s stands for the sth bound-exciton level. τ_{the} represents the thermalization time constant to the free-exciton level. $\tau_{\mathrm{FE},s}$ and $\tau_{e\text{-}h,s}$ are, respectively, the capture time constants of free excitons and electron-hole pairs by the binding centers. τ_p is the radiative decay time constant of electron-hole pairs, τ_{rad} the radiative decay time constant of free excitons, and $\tau_{\mathrm{BE},s}$ the radiative decay time constant of bound excitons.

populated nonradiatively from the $|e\text{-}h\rangle$ level, as depicted in Fig. 12. That process takes place during a time scale $\tau_{\rm the}$ which corresponds to the thermalization time of the photogenerated electron-hole pairs to the $|{\rm FE}\rangle$ level. As shown in Fig. 12, the distribution of ''cold'' free excitons can then recombine radiatively during a time scale $\tau_{\rm rad}$ or nonradiatively populate the $|{\rm BE}\rangle_s$ level. The latter process takes place during a time scale $\tau_{{\rm FE},s}$ which corresponds to the capture time of ''cold'' free excitons by the binding centers. On the other hand, the photogenerated electron-hole pairs can also establish a population of ''hot'' free excitons which can recombine radiatively during a time scale τ_p or thermalize down directly to the $|{\rm BE}\rangle_s$ level and contribute to the overall density of bound excitons. The latter process takes place during a time scale $\tau_{e\text{-}h,s}$ which corresponds to the capture time of ''hot'' free excitons by the binding centers, as depicted in Fig. 12. Finally, the population of bound excitons will eventually dissociate by decaying radiatively to the ground level. That process takes place during a time scale $\tau_{{\rm BE},s}$. The rate equations describing the populations corresponding to the $|e\text{-}h\rangle$, $|{\rm FE}\rangle$, and $|{\rm BE}\rangle_s$ levels are given by

$$\frac{dN_{e\text{-}h}}{dt}=-\frac{N_{e\text{-}h}}{\tau_p}, \tag{23}$$

$$\frac{dN_{\rm FE}}{dt}=\frac{N_{e\text{-}h}}{\tau_{\rm the}}-\frac{N_{\rm FE}}{\tau_{\rm rad}}, \tag{24}$$

$$\frac{dN_{{\rm BE},s}}{dt}=\frac{N_{e\text{-}h}}{\tau_{e\text{-}h,s}}+\frac{N_{\rm FE}}{\tau_{{\rm FE},s}}-\frac{N_{{\rm BE},s}}{\tau_{{\rm BE},s}}, \tag{25}$$

where $N_{e\text{-}h}$, $N_{\rm FE}$, and $N_{{\rm BE},s}$ are, respectively, the densities of photogenerated electron-hole pairs, free excitons, and bound excitons at time t. At $t=0$ s, it is assumed that free excitons are not created and that donor centers do not bind excitons. The solution of the coupled equations (23) to (25) for $N_{{\rm BE},s}$ is given by

$$N_{{\rm BE},s}(t)=\sum_{i=1}^{2} C_{{\rm BE}_i,s}\exp\left(-\frac{t}{\tau_{{\rm BE},s}}\right)-C_{{\rm BE}_1,s}\times\exp\left(-\frac{t}{\tau_{\rm rad}}\right)-C_{{\rm BE}_2,s}\exp\left(\frac{-t}{\tau_p}\right), \tag{26}$$

$$C_{{\rm BE}_1,s}=\left[\frac{1}{\tau_{e\text{-}h,s}}-\frac{\tau_p\tau_{\rm rad}}{\tau_{\rm the}\tau_{{\rm FE},s}(\tau_{\rm rad}-\tau_p)}\right]\frac{N_{e\text{-}h}(0)\tau_p\tau_{{\rm BE},s}}{(\tau_{{\rm BE},s}-\tau_p)}, \tag{27}$$

$$C_{{\rm BE}_2,s}=\frac{N_{e\text{-}h}(0)\tau_p^2\tau_{\rm rad}\tau_{{\rm BE},s}}{\tau_{\rm the}\tau_{{\rm FE},s}(\tau_{\rm rad}-\tau_p)(\tau_{{\rm BE},s}-\tau_p)}, \tag{28}$$

where it is assumed that $\tau_{\rm rad}>\tau_p$, $\tau_{{\rm BE},s}>\tau_p$, and $\tau_{{\rm FE},s}>\tau_{\rm rad}$. The bound-exciton PL which is proportional to the density of bound excitons is thus of the form

$$I_{{\rm BE},s}(t)=\sum_{i=1}^{2} C_{{\rm BE}_i,s}\exp\left(-\frac{t}{\tau_{d,s}}\right)-\sum_{i=1}^{2} C_{{\rm BE}_i,s}\exp\left(-\frac{t}{\tau_{r_i,s}}\right), \tag{29}$$

where $\tau_{d,s}$ is the decay lifetime constant and $\tau_{r_i,s}$ is the ith rise time constant. The parameters $C_{{\rm BE}_i,s}$, $\tau_{r_i,s}$ ($i=1$ or 2), and $\tau_{d,s}$ will be determined from our data analysis. Equation (29) represents a triple-exponential model which reduces to a standard double-exponential model if we set $C_{{\rm BE}_2,s}=0$. Figure 13 displays the PL transient behaviors (circles) of selected lines c, g, j, $k=(k_1,k_2,k_3)$ shown in Fig. 3. The experimental curves display a range of fast components between $\approx$2 and 5 ns, and slow components between $\approx$8 and 48 ns. The decay lifetime constants $\tau_{d,s}$ across (D_2^0,X) have been recently determined for sample 1.[15] The solid lines displayed in Fig. 13 represent least-squares fits obtained using a double-exponential model with $C_{{\rm BE}_1,s}$ and $\tau_{r_1,s}$ as the only fitting parameters. As shown in Fig. 13, the double-exponential model describes remarkably well the transient behavior of the PL curves in a broad $E_{B,X}$ spectral range. The model yields the following rise time and lifetime constants: $\tau_{r_1,c}\approx\tau_{r_1,g}\approx\tau_{r_1,j}\approx\tau_{r_1,k_1}\approx 769$ ps, $\tau_{r_1,k_2}=1.8$ ns, $\tau_{r_1,k_3}=2.6$ ns, $\tau_{d,c}\approx\tau_{d,g}\approx\tau_{d,j}\approx 2.4$ ns, $\tau_{d,k_1}=3.9$ ns, $\tau_{d,k_2}=12.8$ ns, and $\tau_{d,k_3}=24.9$ ns. As shown in the upper panel of Fig. 14, when $E_{B,X}$ is smaller than $\approx$5 meV, the values of $\tau_{r_1,s}$ do not change significantly. However, when excitons bind to deeper binding centers, $\tau_{r_1,s}$ varies linearly with $E_{B,X}$ in a broad $E_{B,X}$ spectral range of $\approx$12 meV,

$$\tau_{r_1,s}=C_{r_1,s}E_{B,X}, \tag{30}$$

where $C_{r_1,s}$ is a rise time proportionality constant. In addition, as displayed in the upper panel of Fig. 14, when $E_{B,X}$ is increased above $\approx$18 meV, $\tau_{r_1,s}$ deviates from its linear behavior and exhibits some kind of saturation at $\approx$2.7 ns, a value close within experimental uncertainty to that of $\tau_{\rm rad}\approx 2.4$ ns. As already mentioned, the behavior of $\tau_{d,s}$ with $E_{B,X}$ has been extensively discussed elsewhere,[15] and is presented in the lower panel of Fig. 14 for comparison purposes. $\tau_{d,s}$ is known to follow a power-law dependence with $E_{B,X}$,

$$\tau_{d,s}=C_{d,s}E_{B,X}^{3/2}, \tag{31}$$

where $C_{d,s}$ is a lifetime proportionality constant. The solid lines of Fig. 14 have been generated using Eq. (30) with $C_{r_1,s}=0.16$ ns meV^{-1} and using Eq. (31) with $C_{d,s}=0.35$ ns meV$^{-3/2}$. Good overall agreement is obtained for a broad $E_{B,X}$ spectral range between experiment and Eqs. (30) and (31). The behavior of $\tau_{r_1,s}$ with $E_{B,X}$ is quite intriguing. Despite the high quality of the fits achieved with a double-exponential model, our results cannot be reconcile with such a simple model which requires that $\tau_{r_1,s}=\tau_{\rm rad}\approx 2.4$ ns. In order to explain our experimental results, the full Eq. (29) should be used. The dotted curves of Fig. 13 have been obtained using Eq. (29) with $\tau_{r_1,s}=\tau_{\rm rad}=2.4$ ns and $\tau_{r_2,s}=\tau_p=769$ ps, and taking $C_{{\rm BE}_1,s}$ and $C_{{\rm BE}_2,s}$ as the only fitting parameters. As displayed by the dotted lines of Fig. 13, the triple-exponential model describes remarkably well the transient behavior of the (D_2^0,X) emission band. As shown in the upper panel of Fig. 14, the results of the fits to the TRPL data achieved with the triple-exponential model revealed that $C_{{\rm BE}_2,s}/C_{{\rm BE}_1,s}\approx C^{te}$ (squares) in a broad $E_{B,X}$ spectral range.

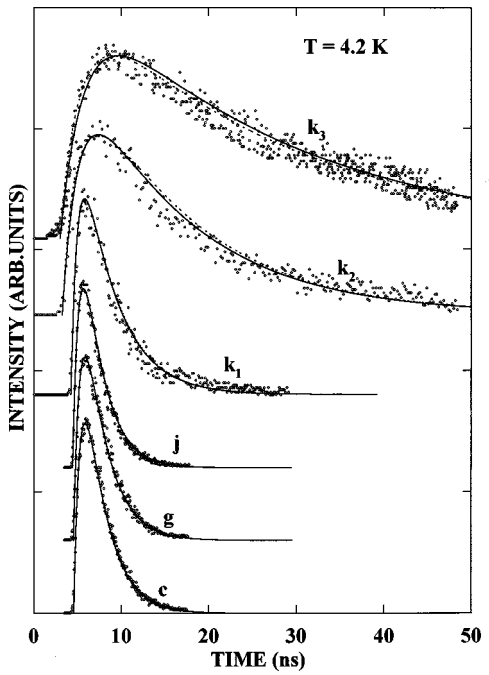

FIG. 13. 4.2-K PL transient measurements (circles) of selected lines shown in Fig. 3 under identical experimental conditions. The solid (dotted) lines are least-squares fits to the data obtained using a double-exponential model (triple-exponential model).

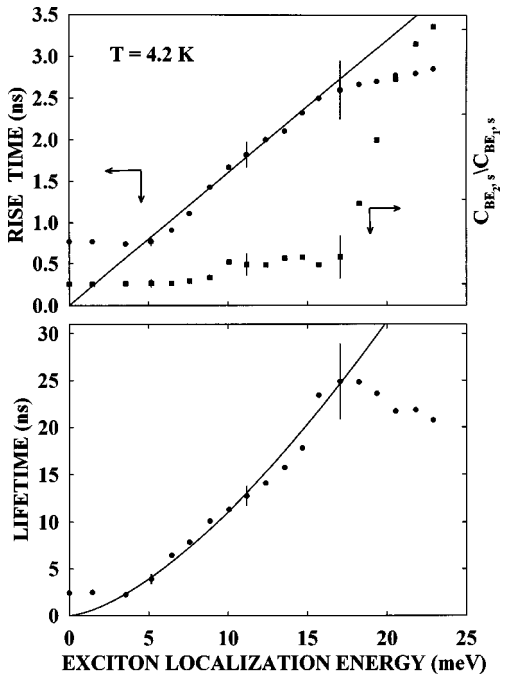

FIG. 14. The upper and lower panels show, respectively, the rise time and lifetime constants across structure *k* of Fig. 3 (circles). The solid curves are fits to Eqs. (30) and (31). The results of the fits obtained using a triple-exponential model are also displayed in the upper panel (squares).

That result seems to indicate that when $E_{B,X}$ increases, both ''cold'' and ''hot'' free-exciton distributions contribute equally to the overall density of bound excitons. In brief, the analysis of our TRPL data revealed that $\tau_{r_{1,s}} \propto E_{B,X}$ across the (D_2^0,X) emission band. Furthermore, since $\gamma_{(B,X)_i} \propto \tau_{r_{1,s}}^{-1}$, it can then be argued that in a diluted system the deeper the binding center, the smaller its corresponding exciton trapping probability. In other words, excitons tend to favor binding around relatively shallow deep-donor centers. That substantiates why the effect of γ_{BE_2} upon γ_{LPB} occurs in the low-temperature range of 4.2–35 K. Now that the effect of γ_{BE_2} upon γ_{LPB} has been clarified, we next investigate whether or not γ_{LPB} exhibits a linewidth narrowing for temperatures below 4.2 K. We point out that the expected linewidth broadening of γ_{LPB} with decreasing temperature associated with the shallowest population of binding centers is not observed around 1.8 K for samples 1–4. That result seems to indicate that lower-branch polaritons may interact perhaps with even shallower neutral donor–bound-exciton complexes than the $(D_1^0,X)_{n=1}$ ones. We point out that in order to probe as a function of temperature the net linewidth narrowing of the LPB associated with the shallowest population of bound excitons, PL measurements must be performed in a quite narrow temperature range well below 1.8 K. We stress the fact that the experimental procedure to carry out such optical measurements is not clear.

Figure 15 shows the typical result of our phenomenological model by displaying the different contributions to γ_{LPB} and γ_{UPB} for sample 1. Regarding samples 1 and 2 (not shown), the main contributions to γ_{UPB} come from $\gamma_{D_1^+}$ and γ_A. The temperature dependencies of γ_{LPB} for samples 1 and 2 are strikingly different. For temperatures below $\approx$25 K ($\approx$15 K) for sample 1 (sample 2), γ_{BE_2} dominates. Regarding sample 1, above $\approx$20 K, excitons dissociate from their deep binding centers and γ_{BE_2} decreases rapidly. For temperatures above $\approx$15 K, sample 2 shows a similar decrease of γ_{BE_2} but linked to the dissociation of excitons from shallower deep binding centers. Above $\approx$70 K, γ_O contributes to both γ_{LPB} and γ_{UPB}, as shown in Fig. 15. Regarding samples 3 and 4, the main contributions to γ_{LPB} and γ_{UPB} come from $\gamma_{D_1^+}$, γ_A, and γ_O in the temperature range investigated (not shown). We point out that $\gamma_{D_2^+}$ contributes weakly to both γ_{LPB} and γ_{UPB} in all our samples since the deep-donor centers are mostly neutral for temperatures below 80 K.

In order to explain quantitatively the temperature dependencies of γ_{LPB} and γ_{UPB}, the polariton interaction with bound excitons, ionized impurities, and phonons must be taken into account. However, the rigorous theoretical calculation of such interactions is difficult to determine within the framework of the polariton transport model. Nevertheless, in a more qualitative approach, the polariton interactions with other crystal excitations can be modeled by introducing in Eq. (1) a phenomenological damping factor Γ^2,

$$\epsilon(k_R+ik_I,E)=\epsilon_b+\frac{4\pi\beta E_n^2(k_R+ik_I)}{E_n^2(k_R+ik_I)-E^2-iE\Gamma}, \qquad (32)$$

where k_R and k_I are, respectively, the real and imaginary polariton wave vectors. k_R describes the normal propagating modes in the crystal, while k_I describes the absorption process of polaritons in the semiconductor since $\alpha=2k_I$, α being the absorption coefficient. Although we realize that the phenomenological approach based on Eq. (32) is question-

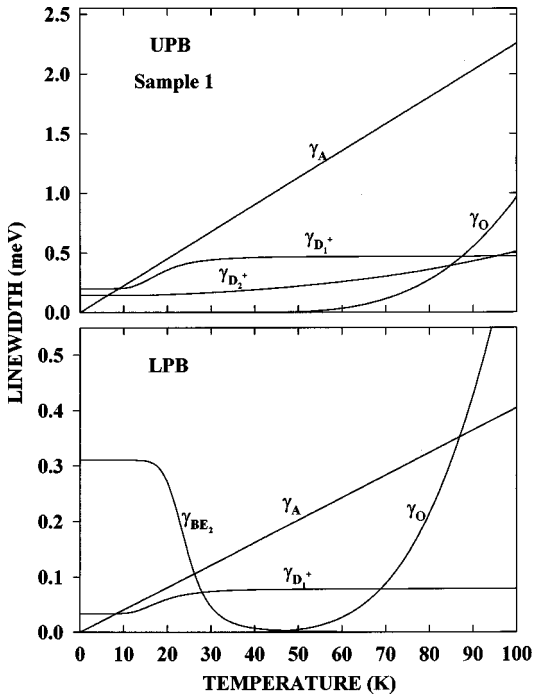

FIG. 15. Contributions to the linewidths γ_{LPB} and γ_{UPB} as a function of temperature (sample 1). $\gamma_{D_1^+}$ and $\gamma_{D_2^+}$ are, respectively, the contribution to the linewidth from shallow and deep impurities. γ_A and γ_O are, respectively, the contribution to the linewidth from LA and LO phonons, and γ_{BE_2} is the contribution to the linewidth from deep-donor bound excitons.

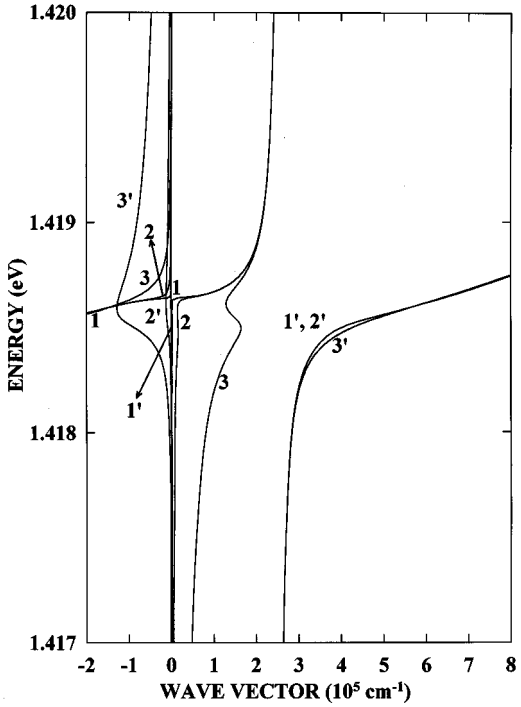

FIG. 16. Real (positive axis) and imaginary (negative axis) LPB (curves $1'$, $2'$, and $3'$) and UPB (curves 1, 2, and 3) dispersion curves of *n*-type InP obtained using Eq. (32) near the exciton resonance as a function of damping. $\Gamma = E_{1,LT}/100$ (curves 1 and $1'$). $\Gamma = E_{1,LT}/10$ (curves 2 and $2'$). $\Gamma = E_{1,LT}$ (curves 3 and $3'$).

able on theoretical grounds, it helps nevertheless describe the transition from undamped to strongly damped polaritons. Figure 16 shows as a function of Γ the imaginary dispersion curves of InP (negative axis). Those curves provide the energy intervals that give rise to optical absorption. On the one hand, the population of photogenerated lower-branch polaritons decreases very rapidly as we depart from the exciton resonance (curves $1'$, $2'$, and $3'$). In addition, the population of photogenerated lower-branch polaritons increases rapidly with increasing Γ (curves $1'$, $2'$, and $3'$). On the other hand, the population of photogenerated upper-branch polaritons slowly decreases as we approach the exciton resonance (curves 1, 2, and 3). Figure 16 also displays the real dispersion curves of InP (positive axis) as a function of Γ. When Γ increases, the LPB dispersion curve is not affected significantly (curves $1'$, $2'$, and $3'$). In contrast, the behavior of the UPB dispersion curve drastically changes by extending at energies below $E_{1,L}$, and at wave vectors smaller than those of the LPB dispersion curve (curves 1, 2, and 3). A density of states which spreads throughout the exciton resonance then becomes available to upper-branch polaritons. We point out that these results are in qualitative agreement with those obtained by Matsuhita near the exciton resonance of CdS.[2] It is to be noted that the results shown in Fig. 16 (positive axis) qualitatively explain the temperature dependencies of γ_{LPB} and γ_{UPB} shown in Figs. 8–11. As already mentioned, our results revealed that γ_{UPB} increases more rapidly as a function of temperature than γ_{LPB}, which does not vary considerably in the corresponding temperature range. In addition, our results can also explain the different values of $\gamma_{(B,X)_2}$ and $\gamma_{D_1^+}$ obtained for samples 1 and 2. It can be argued that a bound-exciton complex is characterized by a short-range scattering potential whereas, in a diluted system, an ionized impurity center is described by a long-range scattering potential. Consequently, polaritons with large wave vectors are more likely to interact with a short-range scattering potential and those with small wave vectors with a long-range one. Moreover, only lower-branch polaritons can have large wave vectors for energies above $E_{1,T}$, as displayed in Fig. 16 (positive axis). Due to the complexity of the polariton picture in semiconductors, it is important to emphasize that the results obtained from Eq. (32) should be used with particular caution. The exact diagonalization of the polariton interactions with the various crystal excitations encounter in this work should help clarify the effect of damping on the dispersion curves of semiconductors. That task is beyond the scope of the present paper, which nevertheless provides insight into the genuine scattering mechanisms that control the emission linewidth in III-V bulk semiconductors such as InP.

IV. CONCLUSION

We have presented a detailed temperature-dependent photoluminescence study of the LPB and UPB components of the $n=1$ free-exciton transition in four high-purity, low-compensation, *n*-type epilayers with a concentration of neutral shallow (deep) donors in the range of $7.9\times10^{13}-2\times10^{15}$ cm^{-3} $[(0-1.45)\times10^{14}$ cm$^{-3}]$. A Lorentzian lineshape analysis of the photoluminescence spectra reveals a process by which the lower-branch polariton population is converted into upper-branch polaritons as the temperature is increased to 25 K. We have also found that the linewidth of

the UPB emission increases more rapidly as a function of temperature than that of the LPB, so that, for high enough temperatures, emissions from both polariton populations coexist in the same energy range. Moreover, when the concentration of neutral deep donors is higher than that of the neutral shallow donors, the emission linewidth from lower-branch polaritons exhibits a striking narrowing in the temperature range of $\approx 10-35$ K due to the polariton interaction with deep-donor bound excitons. In addition, we have observed that the onset of emission linewidth narrowing from lower-branch polaritons shifts to lower temperatures as the neutral shallow-donor concentration is increased but kept below that of the neutral deep donors. That effect is linked to the polariton interaction with a population of shallower deep-donor bound excitons. In contrast, when the concentration of shallow donors is increased significantly above that of the deep donors, the emission linewidth narrowing from lower-branch polaritons vanishes, suggesting that excitons have favored binding around the shallowest donors. That interpretation of the data is supported by the results obtained in a sample free of deep donors, which at low temperatures does not display an emission linewidth narrowing of the LPB. In addition, time-resolved photoluminescence measurements performed across the neutral deep-donor bound-exciton emission band revealed that the rise time constants increase linearly with the exciton localization energy. That result suggests that excitons favor interacting with shallower deep-donor centers, in qualitative agreement with our emission linewidth results corresponding to the lower polariton branch. Taken all together, our results cannot be explained within the framework of the standard polariton transport model, but are nevertheless well reproduced by a phenomenological model which takes into account polariton scattering by bound excitons, ionized impurities, and phonons.

ACKNOWLEDGMENTS

We thank Dr. M. Benzaquen for enlightening discussions concerning the low-field electronic transport analysis, and Dr. Y. Hammoud for calculating the effect of damping on the polariton dispersion curves of InP.

[1] J. J. Hopfield, Phys. Rev. **112**, 1555 (1958).
[2] C. Weisbuch and R. G. Ulbrich, in *Light Scattering in Solids*, edited by M. Cardona and G. Güntherodt (Springer-Verlag, Berlin, 1982), pp. 207–263.
[3] Y. Toyozawa, Prog. Theor. Phys. Suppl. **12**, 111 (1959).
[4] E. S. Koteles *et al.*, Phys. Rev. Lett. **55**, 867 (1985).
[5] T. Steiner *et al.*, Phys. Rev. B **34**, 1006 (1986).
[6] T. Steiner *et al.*, Can. J. Phys. **67**, 242 (1989).
[7] D. J. Wolford *et al.*, in *Physics of Semiconductors: Proceedings of the XXI International Conference, Beijing, China, 1992*, edited by P. Jiang and H. Z. Zheng (World Scientific, Singapore, 1993), p. 241.
[8] R. Benzaquen *et al.*, Phys. Rev. B **50**, 16 964 (1994).
[9] R. Benzaquen *et al.*, Phys. Rev. B **52**, R2273 (1995).
[10] R. Benzaquen, M. Benzaquen, and R. Leonelli, J. Appl. Phys. **82**, 5526 (1997).
[11] M. Benzaquen *et al.*, J. Cryst. Growth **93**, 562 (1988).
[12] R. Benzaquen, A. P. Roth, and R. Leonelli, J. Appl. Phys. **79**, 2640 (1996).
[13] P. Weissfloch, M. Benzaquen, and D. Walsh, Rev. Sci. Instrum. **58**, 9 (1987).
[14] D. L. Rode, in *Transport Phenomena*, edited by R. Willardson and A. Beer (Academic, New York, 1975), Vol. 10.
[15] M. Benzaquen and D. Walsh, Solid State Commun. **89**, 1033 (1994).
[16] R. Benzaquen *et al.*, Phys. Rev. B **53**, 3627 (1996).
[17] S. Rudin, T. L. Reinecke, and B. Segall, Phys. Rev. B **42**, 11 218 (1990).
[18] V. Srinivas, Y. J. Chen, and C. E. C. Wood, Solid State Commun. **89**, 611 (1994).
[19] R. Kubo, *Statistical Mechanics* (North-Holland, Amsterdam, 1965), p. 93.
[20] V. A. Karasyuk *et al.*, Phys. Rev. B **49**, 16 381 (1993).
[21] R. Benzaquen, R. Leonelli, and A. P. Roth, Phys. Rev. B **52**, 1485 (1995).
[22] Y. P. Varshni, Physica (Amsterdam) **34**, 149 (1967).
[23] M. Jaros, F. A. Riddoch, and L. D. Lian, J. Phys. C **16**, L733 (1983).
[24] S. A. Lyon, J. Lumin. **35**, 121 (1986).